Astronomy & Astrophysics manuscript no. aa53432-24
April 22, 2025

Multi-wavelength spectropolarimetric observations of AR13724 performed by GRIS

C. Quintero Noda[1,2], J. C. Trelles Arjona[1,2], T. del Pino Alemán[1,2], C. Méndez Lápido[2], M. J. Martínez González[1,2], T. Felipe[1,2], S. Regalado Olivares[1], P. Gómez González[1], J. Bienes[1], J. Quintero Nehrkorn[1], A. Matta-Gómez[1], M. Barreto[1], and M. Collados[1,2]

[1] Instituto de Astrofísica de Canarias, E-38205, La Laguna, Tenerife, Spain
e-mail: carlos.quintero@iac.es
[2] Departamento de Astrofísica, Univ. de La Laguna, La Laguna, Tenerife, E-38200, Spain

Received 13 December 2024 ; accepted 17 April 2025

ABSTRACT

Multi-line spectropolarimetric observations allow for the simultaneous inference of the magnetic field at different layers of the solar atmosphere and provide insight into how these layers are magnetically coupled. The new upgrade of the Gregor Infrared Spectrograph (GRIS) instrument offers such a possibility, allowing for the simultaneous observation of the Ca II line at 8542 Å, the Si I line at 10827 Å, and the He I triplet at 10830 Å in addition to some additional weaker spectral lines that can probe deeper in the photosphere. Because these spectral lines are sensitive to the plasma properties at different regions of the solar atmosphere, their combined analysis can help understand the stratification of its thermal and magnetic properties from the photosphere to the chromosphere. This work showcases recent observations of the upgraded GRIS at the active region AR13724, which shows the instrument's potential for unravelling the most minute details of solar phenomena. In particular, we analyse the spatial distribution of the polarisation signals as well as the distribution of Stokes profiles for different regimes of the magnetic field strength. We also conduct a preliminary data analysis using relatively simple and approximate methods.

Key words. Sun: magnetic fields, photosphere, chromosphere – Techniques: polarimetric, high angular resolution

1. Introduction

Sunspots are the most prominent solar feature on the visible solar surface and can be observed even by the naked eye. They are magnetic structures where the efficiency of convection is reduced, leading to their lower temperature with respect to the surrounding atmosphere and, in turn, to their appearance as dark features in the photosphere. Generally, sunspots show a dark central region, the umbra, and a less dark surrounding ring, the penumbra. It is in the umbra where the strongest magnetic fields can be found on the solar surface, and these fields are usually oriented close to the local vertical. The magnetic field is typically weaker and more inclined as we move towards the penumbra (for further details, see, for example, the book by Stix 1989 and the reviews by Solanki 2003 and Borrero & Ichimoto 2011, and references therein).

In order to uncover the 3D structure of the magnetic field vector in a sunspot, observations of several spectral lines sensitive to different layers of the solar atmosphere are necessary. Multi-channel spectropolarimetry allows for the simultaneous observation of several spectral lines and is thus an invaluable tool for magnetic field diagnostics. For instance, the Daniel K. Inouye Solar Telescope (Rimmele et al. 2020) and the European Solar Telescope (Quintero Noda et al. 2022) have been designed to allow for these multi-channel observations. This can be achieved by simultaneous observations with multiple instruments specialised in different spectral ranges or by building several spectral channels within a single instrument.

Two main types of instruments are traditionally used for spectro-polarimetric observations of the Sun. Typically based on Fabry-Pérot interferometry, imaging instruments observe a 2D field-of-view (FOV) within a very narrow and tunable wavelength band. They can provide a very high spatial resolution in combination with adaptive optics and image restoration techniques (e.g., Multi-Object Multi-Frame Blind-Deconvolution, Löfdahl 2002; van Noort et al. 2005) and hence have been extensively used by solar observatories. For instance, at ground-based telescopes, examples of this type of instruments are the Telecentric Etalon SOlar Spectrometer (Kentischer et al. 1998), the Interferometric BIdimensional Spectropolarimeter (Cavallini 2006), the CRisp Imaging SpectroPolarimeter (Scharmer et al. 2008), the Gregor Fabry-Pérot Interferometer (Puschmann et al. 2012), the CHROMospheric Imaging Spectrometer (Scharmer 2017), and the Visible Tunable Filter (Schmidt et al. 2014). In balloon missions like Sunrise (Solanki et al. 2010), there is the Imaging Magnetograph eXperiment (Martínez Pillet et al. 2011) and the Tunable Magnetograph (del Toro Iniesta et al. 2025) while, in space, there is, for instance, the Polarimetric and Helioseismic Imager (Solanki et al. 2020) onboard Solar Orbiter. These instruments usually scan one or multiple spectral lines sequentially, recording the solar information at specific spectral positions (usually between 5-15 wavelength points) with a total cadence of 10-20 s per spectral line when performing spectropolarimetric measurements. Their main drawback is the lack of simultaneity of the spectral profiles, as different wavelengths are sampled one after the other. Moreover, the cadence must be bal-

anced with the density of the spectral sampling and the number of spectral lines observed.

Slit spectro-polarimeters observe a spectral region along a line on the plane of the sky (e.g., the Gregor Infrared Spectrograph, GRIS, Collados et al. 2012, or the Visible Spectro-Polarimeter, de Wijn et al. 2022). They can provide spectropolarimetric observations, and by moving the slit, they can scan a 2D FOV while they keep the spectral integrity (i.e., the spectral information is recorded in the sensor at the same time) of profiles. However, the size of the FOV must be balanced with the cadence and degree of spatial simultaneity. In that sense, as the spatial resolution becomes higher thanks to the advent of 4-m class telescopes like DKIST and EST, the time needed to cover a reasonably large spatial domain becomes unattainable and a new type of instrument is needed. The more recently developed Integral Field Spectropolarimeters (IFS) are three-dimensional spectrographs combining the 2D capabilities of imaging instruments and the spectral capabilities of slit spectrographs (see, e.g., Calcines et al. 2013; Iglesias & Feller 2019). As a result, they provide spectra that are simultaneous in both spatial and spectral domains. Also, as IFS can perform observations over a two-dimensional field-of-view strictly simultaneously, they can take advantage of image restoration techniques to improve image quality (Leenaarts et al. 2025). Another benefit of scanning a 2D FOV, albeit small, is that IFS instruments can compensate for atmospheric refraction as imaging instruments traditionally do. Their main drawback is that IFS cover the same 3D information as their long-slit counterpart. This means that for the same sensor, the elongated and narrow FOV of the long slit becomes a much smaller (compared to the long side of the slit) rectangular FOV in the case of the IFS. Several types of IFS systems have been successfully tested in solar physics in recent years, such as a subtractive double pass (e.g., Beck et al. 2018; Mein et al. 2021); image slicers; microlens arrays; and optical fibres. The micro-lens prototype has been tested at the SST with the microlensed hyperspectral imager instrument (van Noort et al. 2022) and the Helium Spectropolarimeter. In the case of image slicers, one unit is installed at the Gregor telescope (Schmidt et al. 2012; Kleint et al. 2020) as an upgrade of GRIS, and it was the first solar IFS system offered openly to the community since 2019 (Dominguez-Tagle et al. 2022). Also, a second unit has been recently installed at the Diffraction Limited Near Infrared Spectropolarimeter (Jaeggli et al. 2022) as an upgrade over the original optical fibres-based IFS, improving the capabilities of the instrument (Anan et al. 2024).

Recently, GRIS has been upgraded to allow for the simultaneous observation of multiple spectral ranges. The version of the instrument offered in 2024 consists of two different cameras installed in each of the two optical arms (see Regalado Olivares et al. 2024, for the optical design). Later on, a third channel will be commissioned as well. One of the possible configurations for the upgraded GRIS instrument is to simultaneously observe the Ca II line at 8542 Å (channel 2) and the spectral region, including the Si I line at 10827 Å and the He I triplet at 10830 Å (channel 1). The Si I line is sensitive in the upper photosphere, the Ca II line is sensitive to the lower and middle chromosphere (see, e.g., Quintero Noda et al. 2016), and the He I triplet is useful for the study of filaments and prominences (e.g., Kuckein et al. 2012; Orozco Suárez et al. 2014; Martínez González et al. 2015), spicules (e.g., Beckers & Tallant 1969; Orozco Suárez et al. 2015), and the on-disk chromosphere (e.g., Solanki et al. 2003; Centeno et al. 2009; Schad et al. 2013). Consequently, combining these spectral lines provides coverage over an extensive range of heights in the solar atmosphere.

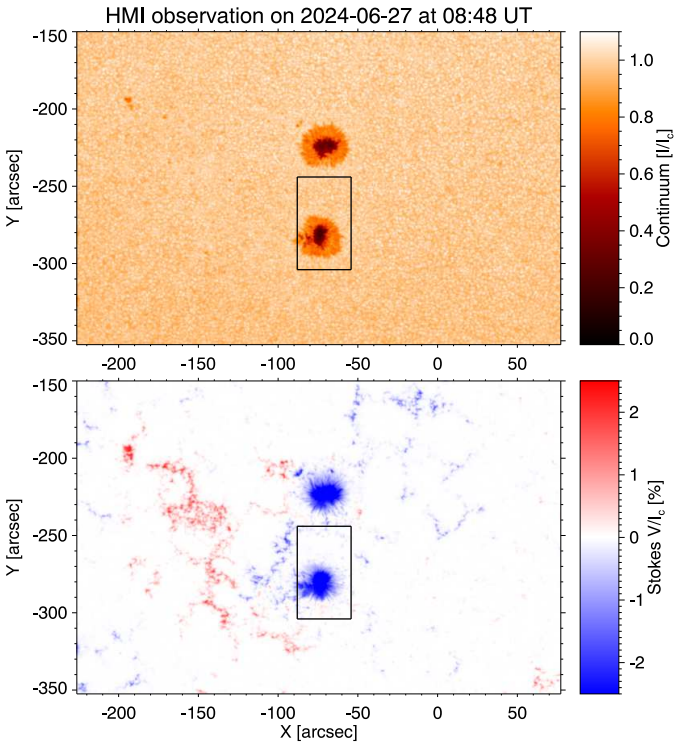

Fig. 1. Continuum intensity map near the Fe I line at 6173 Å (top panel) and Stokes V polarity map for the same spectral line (bottom panel) acquired by the HMI/SDO on 2024 June 27 at 08:48 UT. Both quantities are normalised to the averaged continuum intensity over a quiet Sun area at the disc centre, I_c. The black square delimits the field of view of our observations with the GRIS instrument.

The upgraded GRIS started its commissioning in early 2024 (albeit with only the long-slit configuration available), and so far, it has been delivering high spatial and spectral resolution observations with high polarimetric sensitivity (Quintero Noda et al. 2024b). Moreover, the instrument will offer the option of observing using the integral field unit (as an IFS), hence, the most capable observation mode GRIS can offer from early 2025 on.

2. Data description

We observed AR13724 with GRIS on 2024 June 27, at 08:50 UT. The active region was close to the disc centre at around $(-76, -240)$ arcsec, at a heliocentric angle of $\mu = 0.96$. The observed sunspot was relatively close to another spot with the same polarity as seen in Fig. 1 that displays the observation by the Helioseismic Magnetograph Imager (HMI, Scherrer et al. 2012) onboard the Solar Dynamics Observatory (SDO, Pesnell et al. 2012). Both sunspots exhibit a rounded shape and a clear penumbra. There were no nearby sunspots with opposite polarity, and their companion polarity is thus the active plage to the left of both sunspots. Our observation includes only the sunspot at the bottom (see black square in Fig. 1 delimiting our FOV).

The observation consisted of a long-slit scan with 250 positions with a step of 0.″135. The slit is 60.″48 long, with a sampling of 0.135 arcsec/pix over 448 pixels. The FOV covered by the scan is thus roughly 34×60 arcsec^2 (see Fig. 2). The spatial scale is not strictly the same in the two spectral channels, being about 0.130 arcsec/pix for channel 2. We thus re-scaled the ob-

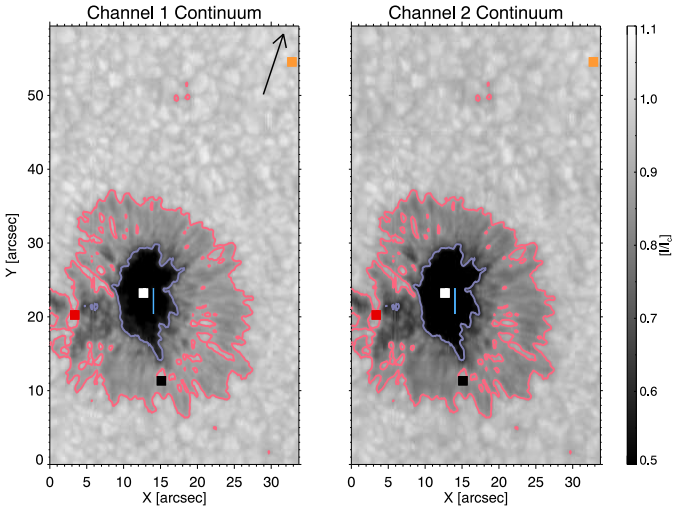

Fig. 2. Spatial distribution of the continuum intensity normalised to the averaged continuum intensity over a quiet Sun area located at the top of the observed field of view, I_c. Panels represent the recorded intensity in channels 1 (left panel) and 2 (right panel) of GRIS. The long-slit scan was performed from the left to right side of the image. The vertical axis corresponds to the north-south direction of the Sun. The coloured symbols highlight regions of interest studied in Section 3. At the same time, contours aim to tentatively underline the location of the umbra (defined as regions with $I_c \sim 0.6$) and the penumbra (areas where $I_c \sim 0.8$). The arrow in the left panel points towards the disc centre.

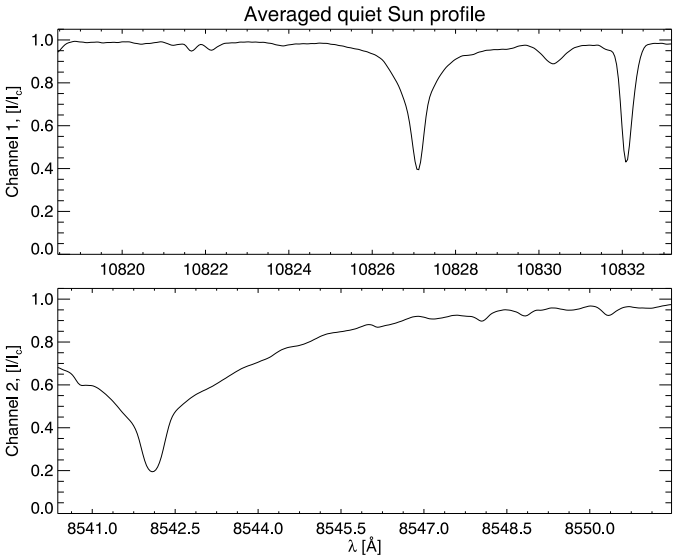

Fig. 3. Average quiet Sun intensity profile, normalised to the average quiet Sun continuum intensity, in channels 1 (top panel) and 2 (bottom panel). The average is taken from the quieter area at the top of the observed FOV (see Figures 1 and 2).

servations from the second channel to match the spatial scale of the first channel.

Figure 3 shows the spectral range of the two optical channels of the GRIS instrument. The new channel 2 is centred at 8547 Å and includes most of the Ca II line at 8542 Å. Channel 1 is centred at 10825.75 Å and covers the Si I line at 10827 Å and the He I triplet at 10830 Å. The spectral coverage is about 15 and 11 Å for channels 1 and 2, respectively. The spectral sampling is about 14.7 and 11.1 mÅ for channels 1 and 2, respectively. To improve the signal-to-noise ratio, we binned the profiles along the spectral domain every three pixels, resulting in a spectral sampling of about 44.1 and 33.3 mÅ for channels 1 and 2, respectively.

We performed a modulation with four polarisation stages (Collados et al. 2012; Quintero Noda et al. 2024a) with an integration of 100 ms each, resulting in 400 ms for each modulation cycle. For each slit position, we acquired ten modulation cycles (i.e., ten accumulations), so each slit position takes about 4 s. For 250 steps, the total observing time was about 30 min (including the additional time required to move the slit). The reference direction for the linear polarisation corresponds to positive Q in the solar south-north direction. We estimate that the noise at continuum wavelengths is of about 9, 11, and 8.5 in units of 10^{-4} the quiet Sun continuum intensity for Stokes Q, U, and V, respectively, for channel 1, and of about 13, 15, and 15 for channel 2, in the same units.

We note that the observation does not reach the continuum in channel 2, which is beyond the 8551.45 Å limit. To normalise the profiles in channel 2 to the average quiet Sun continuum intensity, we assumed for this last wavelength the same relative intensity with respect to the continuum as in the BAse de données Solaire Sol (BASS2000) solar spectrum (Delbouille et al. 1973). In addition, the set-up for the second spectral channel may look suboptimal, with the Ca II line centre significantly shifted to the left side of the spectral range. The reason for this is partly optomechanical. The current configuration is part of the preparation for a possible three-channel configuration (the third channel would be at 7700 Å, covering the K I D_1 line, combined with the configuration shown in this work). The space in the spectrograph and size of the optical components do not allow for better centring of the Ca II line when also observing the He I triplet. Nevertheless, once the third channel is available, it will be possible to use only two of the channels to observe the Ca II and He I lines centred on their respective detectors.

Moreover, because we are observing with the long slit mode of GRIS, we need to consider the impact of the differential atmospheric refraction to discuss the simultaneity of the observations in the two spectral ranges. We have estimated the spatial difference at the date and time of our observation between the two wavelength regions, which is approximately 0.28 arcsec in the case that the shift induced by the atmospheric refraction is strictly perpendicular to the slit. However, when comparing the spatial distribution of intensity signals at the continuum wavelengths of both spectral windows, we obtain the highest correlation when we shift one image with respect to the other 0.135 arcsec horizontally (along the scanning direction). This size corresponds to one slit position, e.g., around 7 s time difference between the two spectral channels. Thus, we consider that we are in a favourable scenario where atmospheric refraction has a low impact on the multi-wavelength configuration used in this work. However, we also want to clarify that a worse scenario can appear when the spectral regions are further apart or the telescope conditions (e.g., a lower elevation) are less favourable. Finally, we also want to note that the GRIS instrument can be configured as an IFS to avoid this limitation. This IFS configuration will be offered starting the first semester of 2025.

3. Spatial and spectral features

In this section, we analyse the spatial distribution of the intensity and the polarisation signals for the three spectral lines mentioned in section 2. We also delve into their characteristic Stokes profiles corresponding to different areas of interest in the FOV,

namely in the quiet Sun, the penumbra, the umbra, and a light bridge-like area.

3.1. Spatial distribution

Figure 4 shows the spatial distribution of the line core intensity, the maximum total linear polarisation (calculated as $LP = \sqrt{Q^2 + U^2}$), and the maximum circular polarisation in absolute value, for the Si I 10827 Å, the Ca II 8542 Å, and the He I 10830 Å spectral lines. For the Si I transition (top row), we see the umbra and penumbra surrounded by the reverse granulation pattern. In the Ca II spectral line (middle row), the dark umbra seems to fill a larger area when compared to the Si I map, showing the presence of a thread-like pattern. The thread-like structures in the umbra in the Ca II line seem to be an indication of the presence of umbral flashes (Beckers & Tallant 1969). In the case of the helium line, we detect many areas that resemble the spatial distribution of continuum signals (see Figure 2). Still, there are other regions where we detect dark threaded features, such as those in the bottom left part of the FOV.

The maximum linear polarisation map for Si I presents relatively weak signals in the regions further from the sunspot and the umbra. However, there are relatively intense polarisation signals localised in the penumbra. For Ca II and He I, the linear polarisation signals are generally weak, even in the penumbra, and only some localised regions show signals whose amplitude is above the noise.

The spatial distribution of circular polarisation signals is similar for all the transitions, with significant values in the inner penumbra and localised areas outside the sunspot. Especially for the Si I spectral line, circular polarisation signals are found at positions of enhanced brightness in the line core intensity. Also, while the circular polarisation signals seem dimmer in the umbra, this is just due to its overall smaller brightness and the fact that the spectra are normalised to the averaged quiet Sun continuum intensity. Moreover, the signature of the mentioned thread-like features or umbral flashes can also be seen in the Ca II circular polarisation (see, e.g., de la Cruz Rodríguez et al. 2013) and in the He I line as well (for example, Centeno et al. 2006; Khomenko & Collados 2015). In contrast to the linear polarisation signals, the silicon and calcium lines show strong circular polarisation signals in the upper (northern) part of the umbra, as shown in Figures 2 and 4. This indicates that the magnetic field exhibits different degrees of inclination with respect to the local vertical on each side of the penumbra, as will be seen in section 3.3.2.

3.2. Characteristic profiles

In this section, we showcase the observational capabilities of the upgraded GRIS instrument by showing and analysing spectropolarimetric profiles characteristic of the different features found within the FOV of our sunspot observation (see section 2). In particular, we have selected profiles in the quiet Sun, penumbra, umbra, an umbral flash, and a light bridge-like area.

3.2.1. Quiet Sun

The analysis of polarisation signals in the quiet Sun (e.g., Khomenko et al. 2003; Martínez González et al. 2007; Lagg et al. 2016) is challenging due to the generally small amplitude of the signals (see, for instance, the reviews by de la Cruz Rodríguez & van Noort 2017; Trujillo Bueno & del Pino Alemán 2022). For the polarimetric noise of our observation, namely $\sim 10^{-3} I_c$, most of the quiet Sun is at the level or below the noise. However, in those regions with magnetic field concentrations, such as network patches, as in, for instance, (33, 57) arcsec (see the orange square in Fig. 2), the polarisation amplitude is well above the noise level.

Figure 5 shows the Stokes parameters at the abovementioned position corresponding to a magnetic network pixel. The intensity in the Si I spectral line is similar to that of the average quiet Sun in Fig. 3. The linear polarisation signals are weak and close to the noise level. However, two positive lobes of small amplitude can be barely identified in the Stokes Q profile. The circular polarisation shows an antisymmetric signal with a red lobe wider than the blue one, which displays a larger amplitude instead. The intensity profile for He I is also similar to the average quiet Sun profile in Fig. 3, but it does not exhibit polarisation signals above the noise level. The Ca II intensity profile has an apparent asymmetry and enhanced intensity in its red wing. The linear and circular polarisation signals are detectable as they are slightly above the noise level.

3.2.2. Light bridge-like area

Figure 6 displays the Stokes parameters at (3.4, 20.3) arcsec, the red square in Fig. 2. In this region located to the left of the umbra in the figure, the filamentary pattern of the penumbra is disrupted by a dark feature with bright roundish dots and one elongated bright intrusion, which could be a weak umbra with umbral dots and a light bridge (e.g., Leka 1997). The polarisation signals in the Si I spectral line are significant and above the noise level. Interestingly, although linear polarisation profiles show a small degree of asymmetry in amplitude, the Stokes V signals seem uniform in terms of amplitude and area asymmetries. The He I triplet absorption is stronger than in the quiet region, with signals that are small in linear polarisation but significant in circular polarisation. The Ca II intensity profile shows an apparent asymmetry, likely due to line-of-sight velocity gradients in the underlying atmosphere. Unlike the significant circular polarisation signal, the linear polarisation profiles are relatively weak.

3.2.3. Penumbra

In Fig. 7, we showcase the Stokes profiles at (15.1, 11.3) arcsec, the black square in Fig. 2. This pixel is located in the sunspot penumbra. As expected, the linear polarisation signals are strong in the Si I and Ca II transitions, as the magnetic field is strongly inclined with respect to the local vertical, which is almost parallel to the line of sight (LOS) as the observations are made close to disk centre, in these regions. Circular polarisation is still detected above the noise level, indicating that this dataset may allow us to infer the topology of the magnetic field in sunspots with reasonably high accuracy.

3.2.4. Umbra and umbral flashes

Figure 8 shows the Stokes parameters at (12.7, 23.9) arcsec, the white square in Fig. 2. The Si I intensity profile displays a complex shape, likely due to the significant magnetic field strength. Regarding its polarisation, we observe substantial signals of circular polarisation and weak linear polarisation signals. The presence of the latter indicates that the magnetic field is not fully aligned with the LOS. The absorption in He I is weaker than in the average quiet Sun (see Fig. 3), and only its circular polarisa-

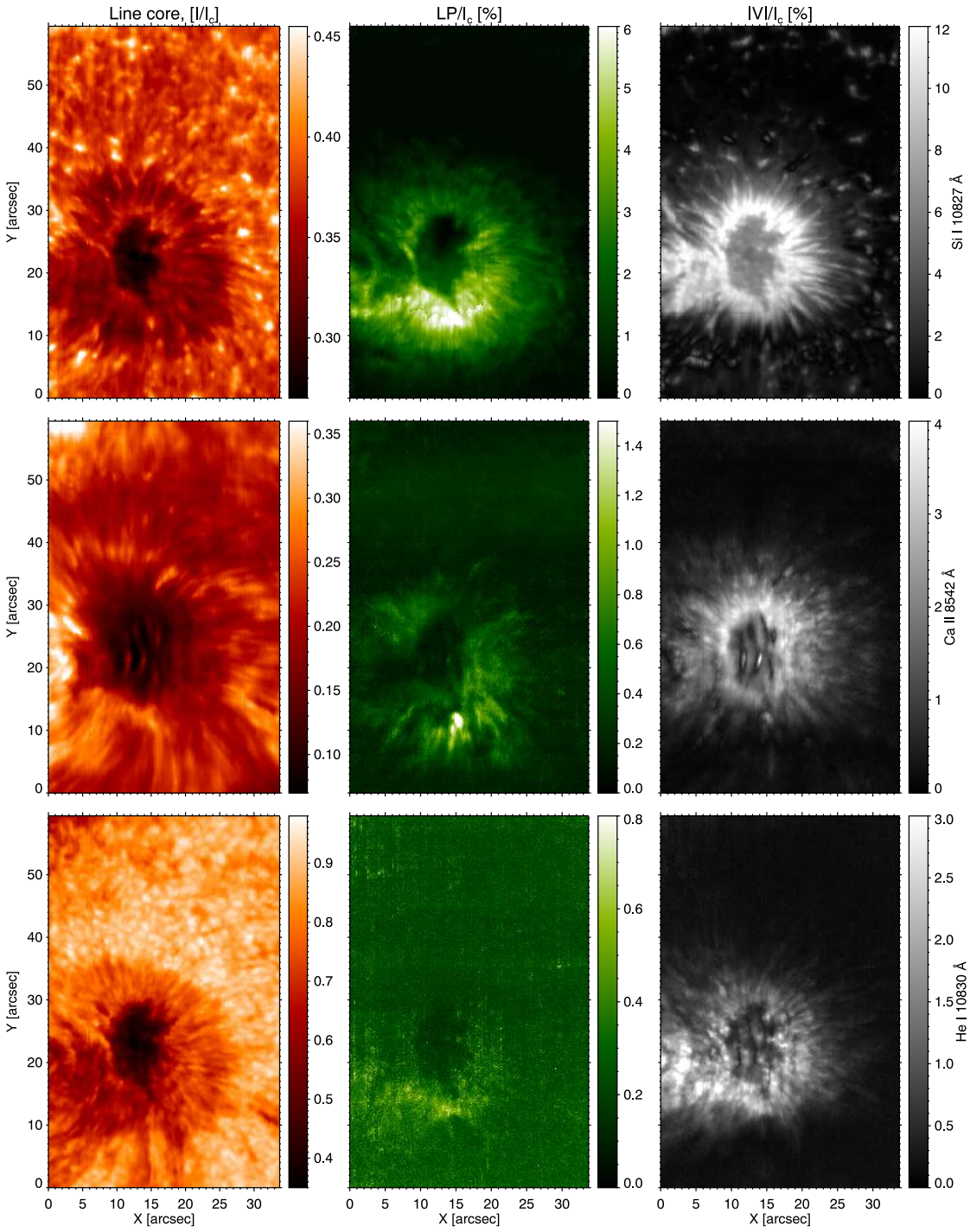

Fig. 4. Spatial distribution of the line core intensity (left column), maximum linear polarisation (central column), and maximum circular polarisation in absolute value (right column) for the Si I line at 10827 Å (top row), the Ca II line at 8542 Å (middle row), and the He I triplet at 10830 Å (bottom row). All quantities are normalised to the average quiet-Sun continuum intensity, I_c.

tion is above the noise level. Finally, in the Ca II spectral line, we only observe significant circular polarisation as the amplitude of the linear polarisation is below the noise level.

While the umbra is predominantly dark when observed in the line centre of the Ca II line, we can see the signature of umbral flashes (see Fig. 4). They are sudden brightenings close to the line core of some chromospheric transitions in sunspot umbrae, produced by acoustic waves travelling upwards from the photosphere and becoming shocks due to the steep fall of the plasma density. Umbral flashes have been thoroughly studied using spectropolarimetric observations with long-slit spectrographs such as the Tenerife Infrared Polarimeter (Collados et al. 2007) at the Vaccum Tower Telescope (von der Lühe 1998) or imaging instruments such as the CRISP at the SST. As examples, we have the works of (e.g., Socas-Navarro et al. 2001; de la Cruz Rodríguez et al. 2013; Henriques et al. 2017; Joshi & de la Cruz Rodríguez 2018) that, except for a few exceptions (Maurya et al. 2013; French et al. 2023), have mainly

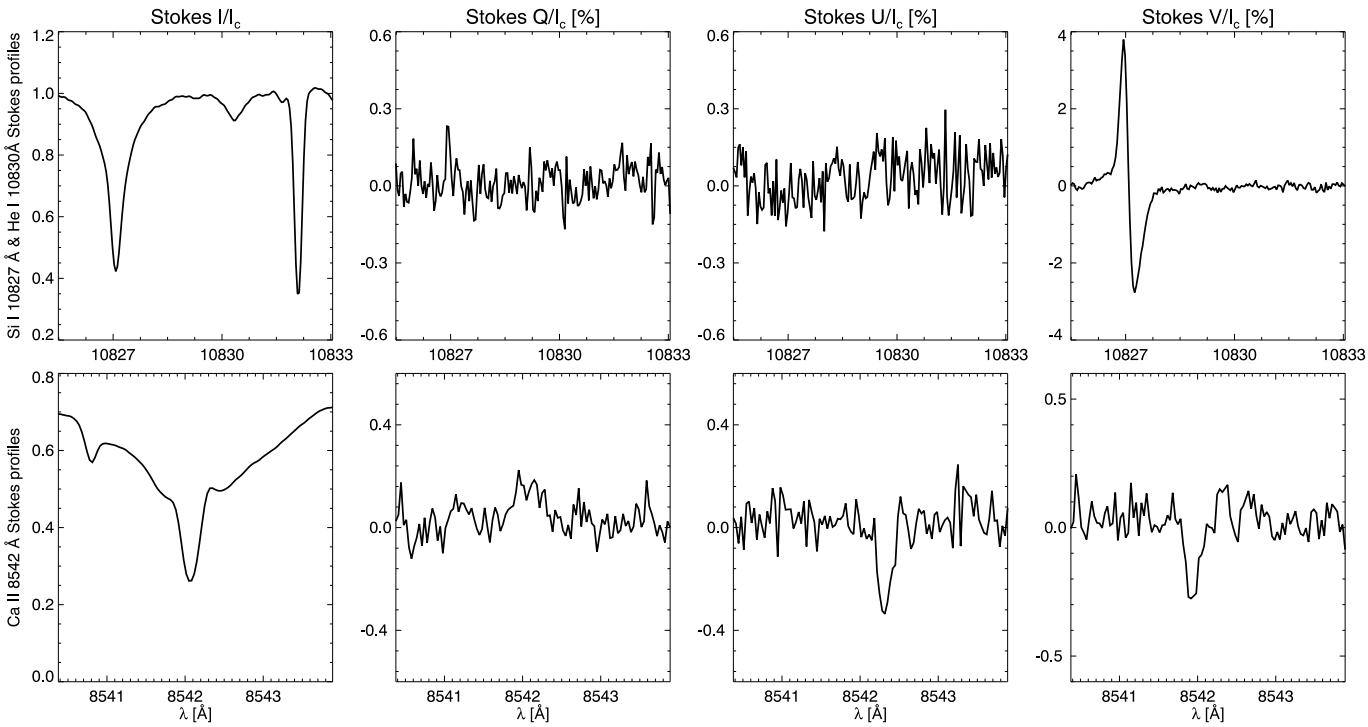

Fig. 5. Intensity (first column), Stokes Q (second column), U (third column), and V (fourth column) profiles, normalised to the average quiet-Sun continuum intensity, I_c. The top row shows the spectra in channel 1, which includes the Si I line at 10827 Å and the He I triplet at 10830 Å. The bottom row shows the spectra in channel 2, which includes most of the Ca II line at 8542 Å. The displayed profiles correspond to the pixel at (33, 57) arcsec, the orange square in Fig. 2, associated with a quiet Sun area with low magnetic activity.

employed imaging spectropolarimeters. One of the drawbacks of imaging instruments is the time-dependent acquisition of the wavelengths along the spectral line, which can produce deformations of the Stokes profiles when the solar atmosphere changes at short temporal scales, as in the case of umbral flashes (Felipe et al. 2018). In this regard, while the particular observation shown in this work is a slit scan, the analysis of umbral flashes using IFS spectrographs such as GRIS can potentially improve our understanding of this phenomenon by providing better spectral resolution and the simultaneous acquisition of all the wavelengths of the spectral line (better spectral integrity).

Figure 9 shows the intensity and circular polarisation profiles for the Ca II, Si I and He I spectral lines along a region of the spectrograph slit at one step of the scan, indicated by the blue segment in Fig. 2. The linear polarisation profiles are not included since their signal is below the noise level. The Si I spectral line and He I triplet do not show any remarkable changes in the selected region of the umbra, something we will study in more detail in the future. In contrast, there is significant variability of the spectra along the slit in the Ca II transition. Towards the borders of this region, the profiles show a similar shape as those from the sunspot dark umbra (see Fig. 8). However, near the centre of the selected region, we observe a striking intensity enhancement at the blue wing of the Ca II line that could be due to the propagation of waves from deeper layers (see, for instance, the series of works that started with Beck et al. 2009). The umbral flash also manifests in the circular polarisation signals. They exhibit three-lobed profiles that still seem to correspond approximately to the first derivative of the intensity profile (see Figure 10) suggesting the applicability of the weak-field approximation (WFA) for analysing the data (Sect. 3.3.2).

3.3. Inferred physical quantities

In this section, we apply relatively simple diagnostic techniques to obtain a first estimation of relevant physical quantities in the solar atmosphere at the region of formation of the observed spectral lines. In particular, we study the velocity along the LOS and apply the WFA to the Stokes profiles to estimate the magnetic field vector. We plan to use more sophisticated inversion techniques for this dataset and present the results in a following publication.

3.3.1. LOS velocities

We compute the velocity along the LOS from the Doppler shift of the line centre of each spectral line with respect to its theoretical line centre (see Fig. 11). We expect this simple approach to be less accurate when the magnetic field strength is such that the Zeeman splitting becomes comparable with the line width, which may happen, e.g., for the Si I line in the umbra. The positive values (red colours) correspond to redshifts.

The velocity along the LOS at the region of formation of the Si I line centre shows a spatial distribution that resembles the granulation pattern. The penumbra and the outer regions of the umbra show small velocities, as expected. The velocity along the LOS at the height of formation of the Ca II line centre shows an umbra dominated by the thread-like shape of the umbral flashes. The velocity in the penumbra shows a filamentary pattern similar to the one observed in the line centre intensity (see Fig. 4). In the top region of the FOV, we see elongated features that are larger in area when compared with the velocity map for Si I. Finally, the spatial distribution of velocities from the He I triplet resembles that of the calcium transition but with larger values and longer extension. The larger velocity values in the He I line

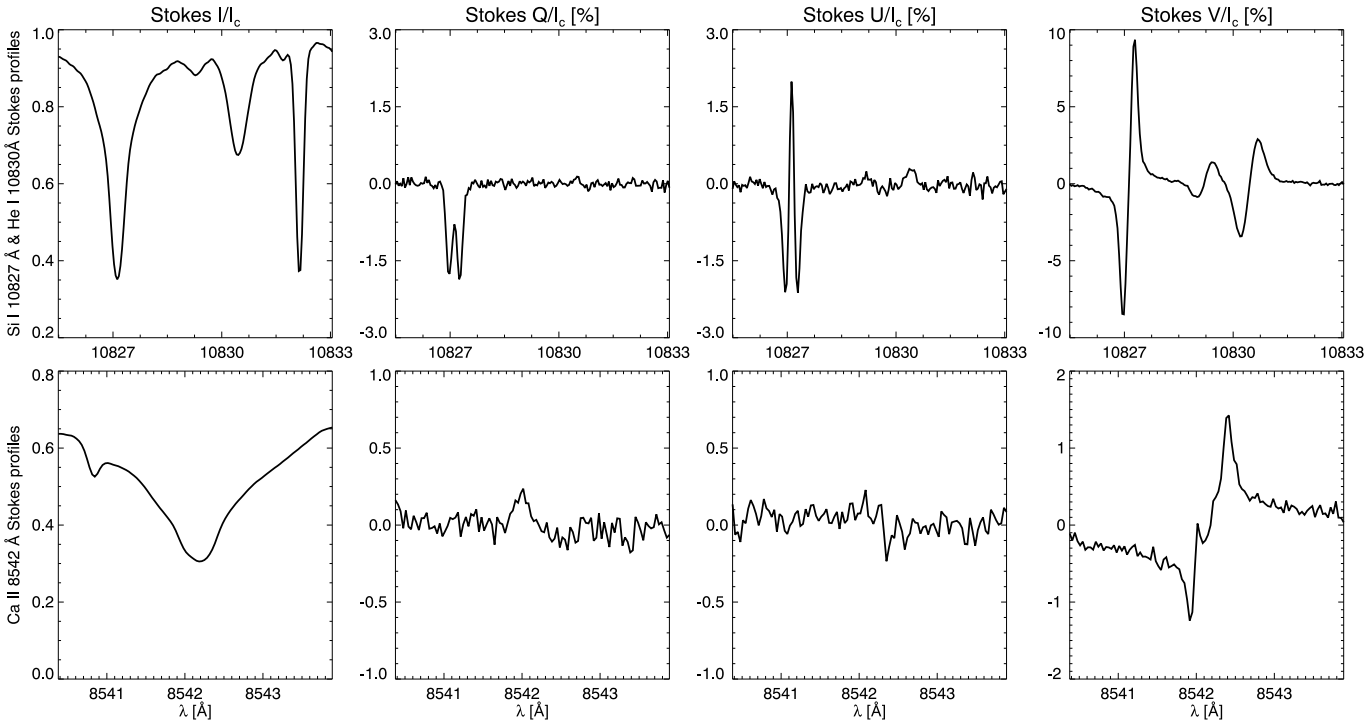

Fig. 6. Same as Fig. 5, but for a pixel in the light bridge-like area at (3.4, 20.3) arcsec, the red square in Fig. 2.

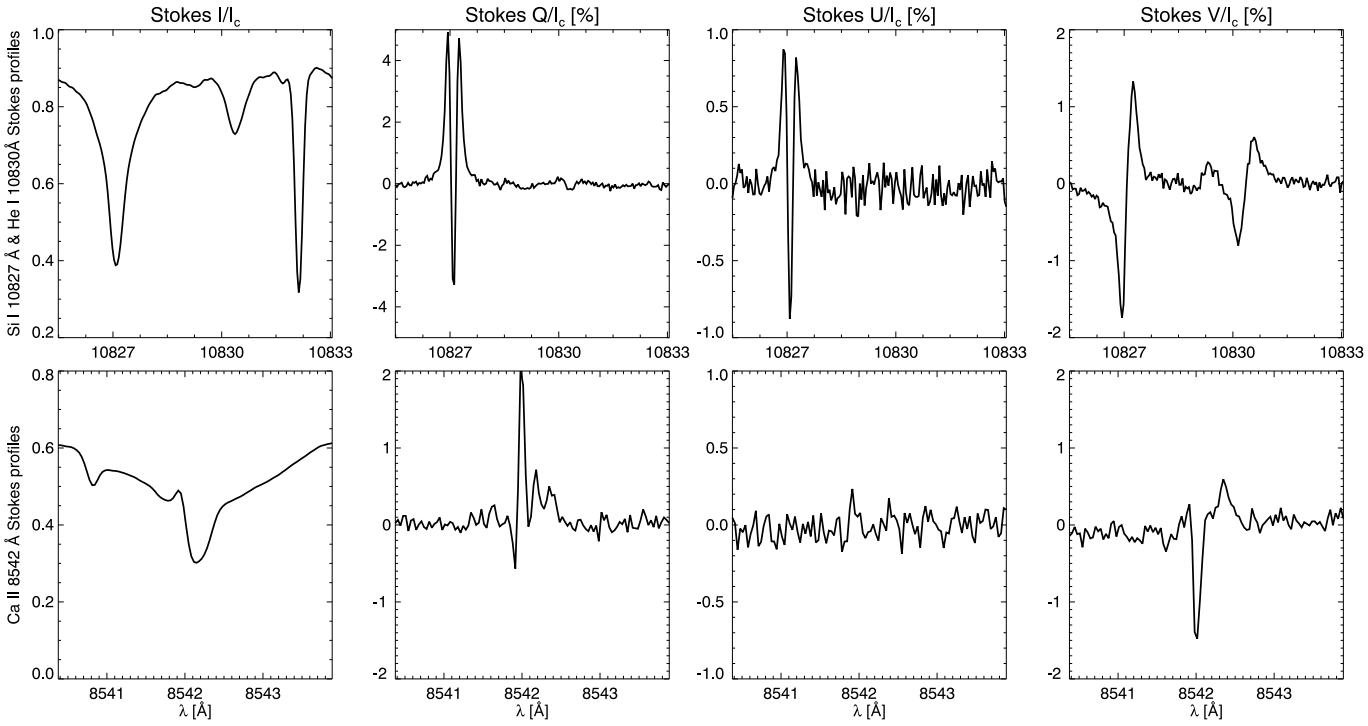

Fig. 7. Same as Fig. 5, but for a pixel in the penumbra at (15.1, 11.3) arcsec, the black square in Fig. 2.

could be due to the higher height of formation and the presence of waves propagating through the atmosphere of the umbra (e.g., Centeno et al. 2006).

3.3.2. Magnetic field vector

The WFA (e.g., Rayrole 1967) equations for the Stokes parameters are obtained from the radiative transfer equations under the assumption that the Zeeman splitting is much smaller than the typical width of the spectral line. Moreover, under the assumption that several physical quantities are constant along the region of formation of the polarisation profiles, it is possible to write

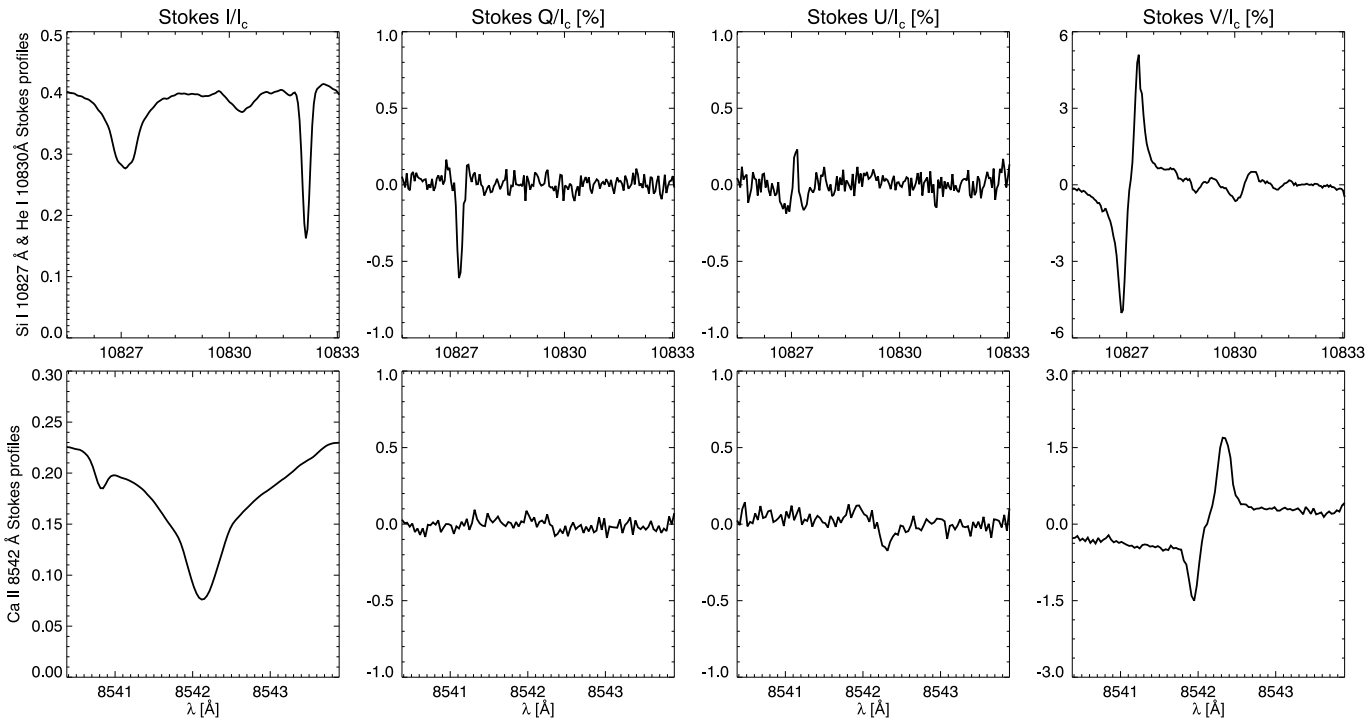

Fig. 8. Same as Fig. 5, but for a pixel in the umbra at (12.7, 23.9) arcsec, the white square in Fig. 2.

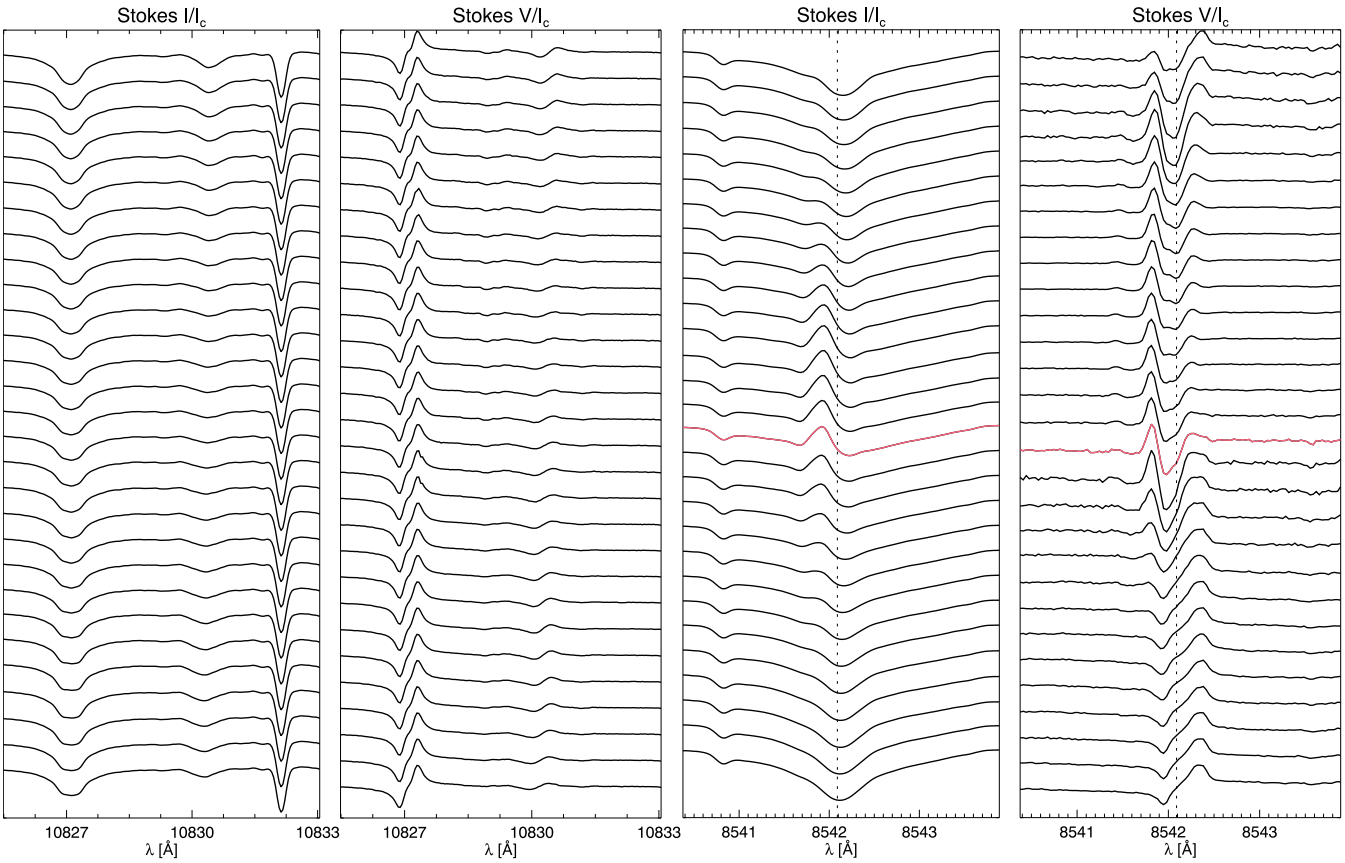

Fig. 9. Intensity (first and third panels from the left) and circular polarisation (second and fourth panels from the left) profiles for channel 1 (first and second panels) and channel 2 (third and fourth panels) for all pixels in a region that covers 4 arcsec (i.e., 29 pixels) along the spectrograph slit indicated with a blue segment in Fig. 2. Red highlights the pixel we study in Figure 10.

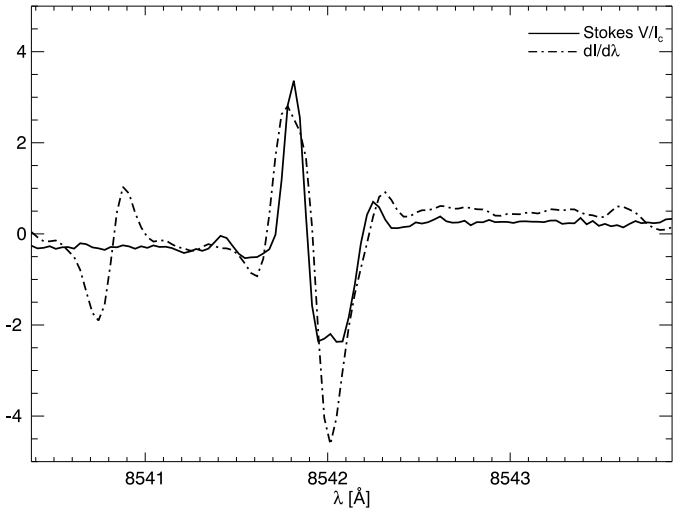

Fig. 10. Comparison between the Stokes V profile (solid) and the derivative of Stokes I with respect to the wavelength. The Stokes profiles are normalised to the quiet Sun averaged continuum intensity, and the representation of Stokes V is in percentage units. At the same time, we scale the derivative with an arbitrary factor to match the Stokes V amplitude. The location of this pixel is highlighted in colour in Figure 9.

closed equations relating the emergent Stokes parameters and the magnetic field vector. These closed equations are (see, e.g., Landi Degl'Innocenti & Landolfi 2004)

$$Q = -\frac{1}{4}C^2 G_{\rm eff}\lambda_0^4 B_\perp^2 \cos 2\phi \frac{\partial^2 I}{\partial \lambda^2}, \tag{1a}$$

$$U = -\frac{1}{4}C^2 G_{\rm eff}\lambda_0^4 B_\perp^2 \sin 2\phi \frac{\partial^2 I}{\partial \lambda^2}, \tag{1b}$$

$$V = -C g_{\rm eff}\lambda_0^2 B_\parallel \frac{\partial I}{\partial \lambda}, \tag{1c}$$

where $B_\parallel$ is the magnetic field component parallel to the LOS, $B_\perp$ is the module of the magnetic field vector in the plane of the sky, ϕ is the azimuth of the magnetic field vector in the plane of the sky, $C = 4.67\cdot 10^{-13}$ G^{-1}Å^{-2}, λ_0 is the line centre wavelength in Å, $g_{\rm eff}$ is the effective Landé factor, and $G_{\rm eff}$ is a number that plays the role of the effective Landé factor for linear polarisation.

Note that Eq. (1c) is only valid if $B_\parallel$ is constant across the region of formation of Stokes V. The restrictions for Eqs. (1a)–(1b) are significantly more strict. They are valid for the line centre if $B_\perp$, ϕ, and the velocity along the LOS are constant across the region of formation. For these expressions to be valid for the whole spectral line, the absorption profile must have a Gaussian shape, and the line widths must be constant with height (see also Centeno 2018). Alternatively, the expressions (Landi Degl'Innocenti & Landolfi 2004)

$$Q = \frac{3}{4}C^2 G_{\rm eff}\lambda_0^4 B_\perp^2 \cos 2\phi \frac{1}{\lambda-\lambda_0}\frac{\partial I}{\partial \lambda}, \tag{2a}$$

$$U = \frac{3}{4}C^2 G_{\rm eff}\lambda_0^4 B_\perp^2 \sin 2\phi \frac{1}{\lambda-\lambda_0}\frac{\partial I}{\partial \lambda}, \tag{2b}$$

are valid in the line wings (at λ such that $|\lambda-\lambda_0|$ is much larger than the Doppler width) if $B_\perp$, ϕ, and the velocity along the LOS are constant in the region of formation.

We calculated the Landé factors for the Si I line at 10827 Å and the Ca II line at 8542 Å by assuming LS coupling as in Landi Degl'Innocenti & Landolfi (2004), that is,

$$g_{\rm eff} = \frac{1}{2}(g_1+g_2) + \frac{1}{4}(g_1-g_2)[J_1(J_1+1) - J_2(J_2+1)], \tag{3a}$$

$$G_{\rm eff} = g_{\rm eff}^2 - \frac{1}{80}(g_1-g_2)^2\left(16s - 7d^2 - 4\right), \tag{3b}$$

where g_i and J_i with $i = 1, 2$ are the Landé factor and total angular momentum of the upper and lower levels of the transition. The Landé factor and the quantities s and d are given by

$$g_i = \frac{3}{2} + \frac{S_i(S_i+1) - L_i(L_i+1)}{2J_i(J_i+1)}, \quad (i = 1, 2) \tag{4a}$$

$$s = J_1(J_1+1) + J_2(J_2+1), \tag{4b}$$

$$d = J_1(J_1+1) - J_2(J_2+1), \tag{4c}$$

with S_i and L_i the spin and orbital angular momenta of the upper and lower levels of the transition.

In Table 1, we show, from left to right, the atomic species, line core wavelength, lower and upper level atomic configuration, Landé factor, effective Landé factor for the circular polarisation, s and d (see Eq. 4b and 4c), and the effective Landé factor for the linear polarisation.

For the He I triplet at 10830 Å the situation is more complex. The red component of the multiplet, which is the one showing polarisation signals in our observations, is a blend of the two transitions listed in Table 1. Consequently, for this spectral line, we calculated $g_{\rm eff}$ by applying the WFA to synthetic profiles obtained with the HAnle and ZEeman Light (HAZEL, Asensio Ramos et al. 2008) code for several known magnetic fields and $\lambda_0 = 10830.34$ Å. While the WFA fit is not perfect due to the blend, the best fit is achieved for $g_{\rm eff} = 1.134$. Also, for the He I line, we have only applied the WFA to the circular polarisation profiles, as the linear polarisation profiles cannot be modelled by considering only the Zeeman effect because there can be a significant contribution by the Hanle effect (Trujillo Bueno & Asensio Ramos 2007).

By assuming Gaussian and uncorrelated noise, we can write the maximum likelihood expressions for $B_\parallel$, $B_\perp$, and ϕ (Martínez González et al. 2012),

$$B_\parallel = -\frac{1}{C\lambda_0^2 g_{eff}}\frac{\sum_\lambda V_\lambda \frac{\partial I(\lambda)}{\partial \lambda}}{\sum_\lambda \left(\frac{\partial I(\lambda)}{\partial \lambda}\right)^2}, \tag{5a}$$

$$B_\perp^2 = \frac{4}{\gamma C^2 \lambda_0^4 G_{eff}^2}\frac{\sqrt{\left(\sum_\lambda Q_\lambda \mathcal{I}\right)^2 + \left(\sum_\lambda U_\lambda \mathcal{I}\right)^2}}{\sum_\lambda \mathcal{I}^2}, \tag{5b}$$

where

$$\begin{cases}\gamma = 1,\\ \mathcal{I} = \frac{\partial^2 I(\lambda)}{\partial \lambda^2},\end{cases} \tag{6}$$

for the line centre, and

$$\begin{cases}\gamma = 3,\\ \mathcal{I} = \frac{1}{\lambda-\lambda_0}\frac{\partial I}{\partial \lambda},\end{cases} \tag{7}$$

for the line wing. We consider for calcium as line wing and line core the ranges [8541.045, 8541.279] and [8541.881, 8542.349] Å, respectively. For the silicon and helium, we consider the range between [10825.050,10828.127] and [10830.017, 10831.644] Å, respectively.

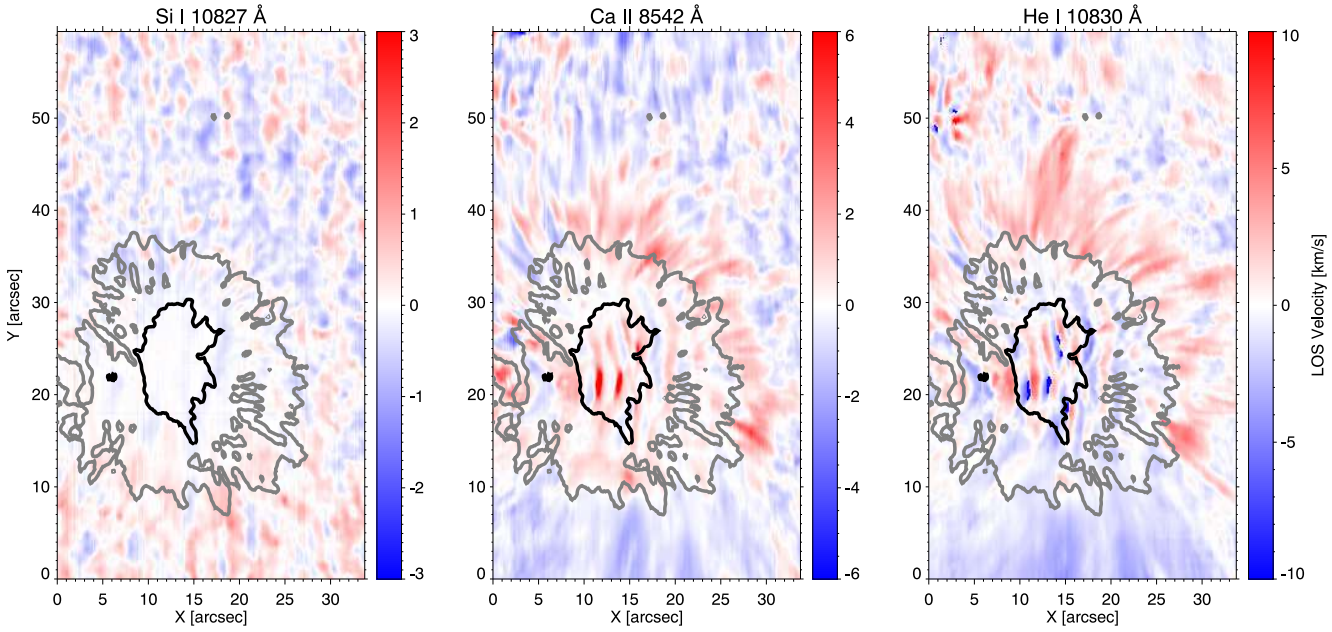

Fig. 11. Spatial distribution of the velocity along the LOS inferred from the Doppler shift of the Si I 10827 Å (left), Ca II 8542 Å (middle), and He I 10830 Å (right) spectral line centres. Contours tentatively define the area corresponding to the umbra and penumbra computed from the continuum intensity maps presented in Figure 2.

Table 1. Effective Landé factor for the linear and circular polarisation.

Atom	λ [Å]	Conf$_1$	Conf$_2$	g_1	g_2	$g_{\rm eff}$	s	d	$G_{\rm eff}$
Ca II	8542.09	$^2D_{5/2}$	$^2P^o_{3/2}$	1.20	1.33	1.10	12.50	5.00	1.205
Si I	10827.091	$^3P^o_2$	$^3P_2$	1.50	1.50	1.50	12.00	0.00	2.250
He I	10830.25	$^3S_1$	$^3P^o_1$	2.00	1.50	1.75	4.00	0.00	2.875
He I	10830.34	$^3S_1$	$^3P^o_2$	2.00	1.50	1.25	8.00	-4.00	1.525

The magnetic field inclination and azimuth in the plane of the sky are given by

$$\Theta = \arctan \frac{B_\perp}{B_\parallel}, \tag{8a}$$

$$\phi = \frac{1}{2} \arctan \frac{\sum_\lambda U_\lambda}{\sum_\lambda Q_\lambda} + \phi_0, \tag{8b}$$

with the conditions for ϕ_0 as defined in Martínez González et al. (2012).

In Fig. 12, we present the parallel and perpendicular components of the magnetic field and the inclination with respect to the LOS (a LOS which is very close to the local vertical as we are close to the disc centre) resulting from the application of Eqs. (5a), (5b), and (8a) to the Si I and Ca II lines in the aforementioned wavelength ranges. In Fig. 13, we show the parallel component of the magnetic field from the application of Eq. (5a) to the He I line in the abovementioned wavelength range. Unlike the Ca II line, the Si I and He I lines are sensitive to the physical parameters of the solar atmosphere in a relatively narrow range of heights, and the inferred $B_\parallel$ does not show significant variation when restricting Eq. (5a) to different wavelength ranges. Thus, we only show one value for the longitudinal magnetic field for these spectral lines. Moreover, as mentioned above, the WFA is not suitable to estimate $B_\perp$ from the He I line due to the potential impact of the Hanle effect on the linear polarisation profiles, particularly on regions where the magnetic field is weak. Given the height of formation of the observed Si I and Ca II lines (see, for instance, Quintero Noda et al. 2024c, 2016, respectively), moving from left to right in Fig. 12 is roughly equivalent to moving up in height in the solar atmosphere.

In the deeper layers, corresponding to the Si I spectral line, we infer a strong $B_\parallel$ (top row in Fig. 12) in the inner penumbra, in the umbra, and the penumbra to the left of the sunspot, with the rest of the penumbra showing weak $B_\parallel$. The rest of the FOV is dominated by weaker $B_\parallel$, with some scattered features corresponding to network concentrations. At the height sampled by the Ca II line wing, $B_\parallel$ has a similar behaviour. Finally, at the regions sampled by the Ca II line centre, there is a thread-like pattern in the umbra produced by the umbral flashes, where the inferred $B_\parallel$ slightly increases with respect to the values at wing wavelengths. This may be due to a change in the height of formation (e.g., the line is sensitive to lower layers in the atmosphere) instead of an actual increase in the magnetic field strength. The magnetic field inferred from the He I line shows a similar spatial distribution (see Fig. 13) where the threaded-like pattern in the umbra due to the presence of umbral flashes becomes one of the most prominent features again.

Regarding the inferred $B_\perp$ (middle row in Fig. 12), it is essential to emphasise that this quantity (and thus the inclina-

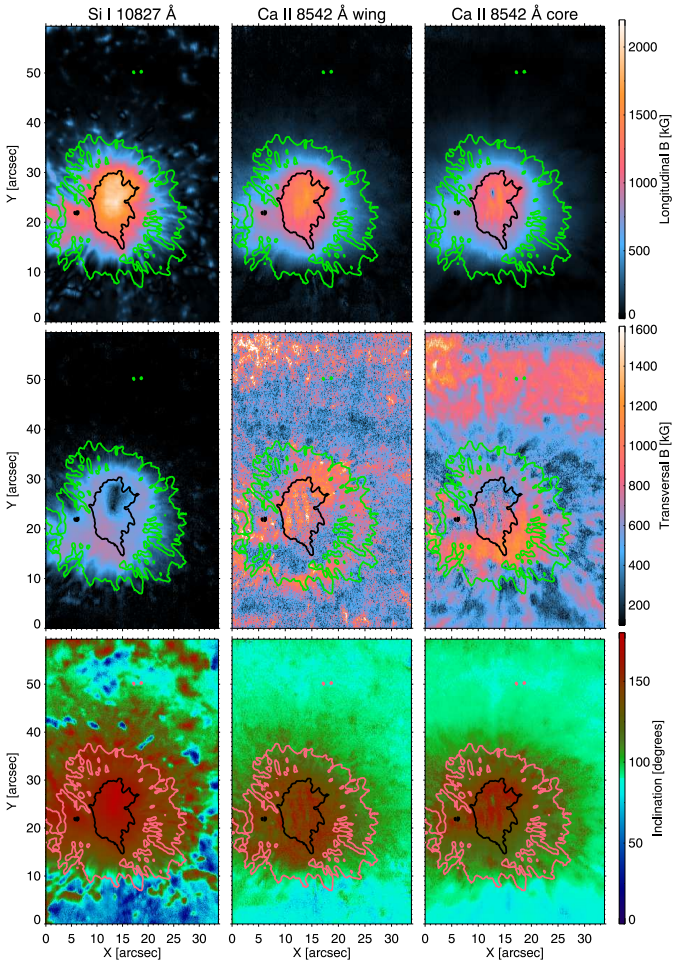

Fig. 12. Spatial distribution of the longitudinal (top row) and transverse (middle row) components of the magnetic field inferred from the WFA on the Si I line (first column) and on the Ca II line wing (second column) and line centre (third column). The bottom row shows the inclination of the magnetic field obtained by applying Eq. 8a to the WFA results. The wavelength ranges considered in the calculations are indicated in the text. Contours tentatively define the area corresponding to the umbra and penumbra computed from the continuum intensity maps presented in Figure 2.

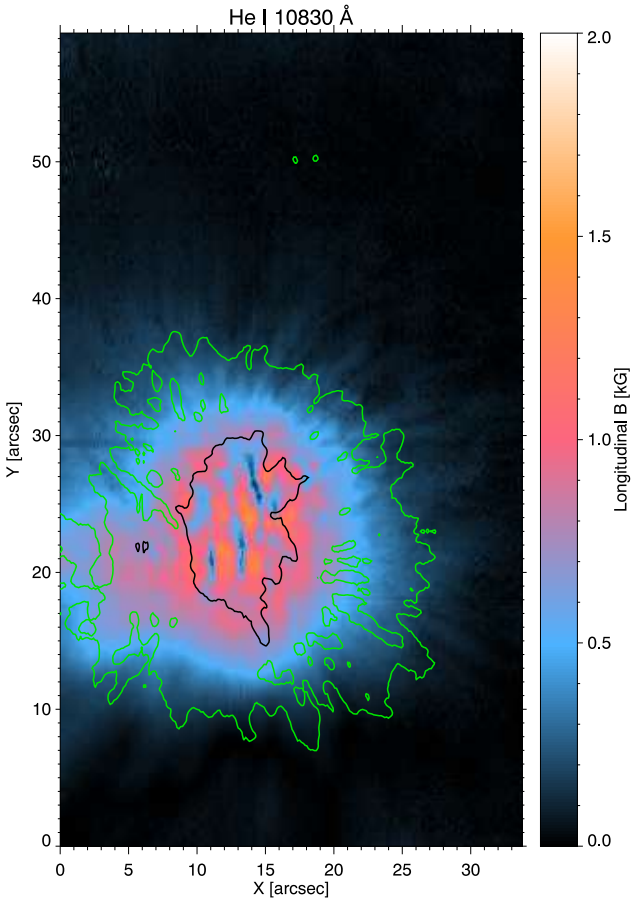

Fig. 13. Spatial distribution of the longitudinal component of the magnetic field inferred from the application of the WFA to the He I line. Contours tentatively define the area corresponding to the umbra and penumbra computed from the continuum intensity maps presented in Figure 2.

tion angle) has a non-zero bias and therefore small $B_\perp$ (at the order or smaller than the noise amplitude) are overestimated (Martínez González et al. 2012). Especially for the Ca II line, the observed linear polarisation signals are below the noise level in a significant amount of pixels (see Fig. 4). At the height sampled by the Si I, we infer relatively strong $B_\perp$ in most of the penumbra and weak values for the inner umbra. The Ca II line wing shows strong $B_\perp$ values in the complex light-bridge-like structure and the penumbra. In contrast, the results from the line centre show significant values in the lower (southern) part of the penumbra. Notably, many quiet Sun areas show a transverse magnetic field in the order of kG for the inferred transverse field for the Ca II line. We do not consider this result plausible for chromospheric quiet Sun magnetic fields, and we believe it is because most of the pixels outside the active region have linear polarisation signals that are close to or below the noise level.

Figure 14 displays the inferred magnetic field azimuth in the plane of the sky. We note that we have not disambiguated the azimuth; thus, the values are in the $[-90°, 90°]$ range. For both the observed Si I and Ca II lines, the inferred azimuth closely follows an expected radial pattern with respect to the centre of the sunspot. Although the values inferred from the Ca II line seem slightly shifted with respect to those corresponding to the Si I line. This could be due to a rotation of the magnetic field with height. Still, more sophisticated inference techniques, which we plan to apply in a forthcoming work, are necessary to confirm this interpretation. Finally, the He I transition only shows linear polarisation signals in the lower part of the penumbra, and the results in this region are only partially consistent with those corresponding to the Si I and Ca II lines. On the one hand, the azimuth values for penumbral regions between $X = [15, 23]$ arcsec seem consistent with those inferred for the other two transitions. On the other hand, values obtained outside the mentioned penumbral region are quite different than those from the other two transitions. Thus, if we consider that the linear polarisation signals for the helium transition are very weak almost everywhere (see Figure 4), we should not pay too much attention to the helium results.

4. Summary

We have presented the new capabilities of the upgraded GRIS instrument. The new two-channel configuration allows for the simultaneous observation of the Ca II line at 8542 Å, the Si I line at 10827 Å, and the He I triplet at 10830 Å, probing a wide region

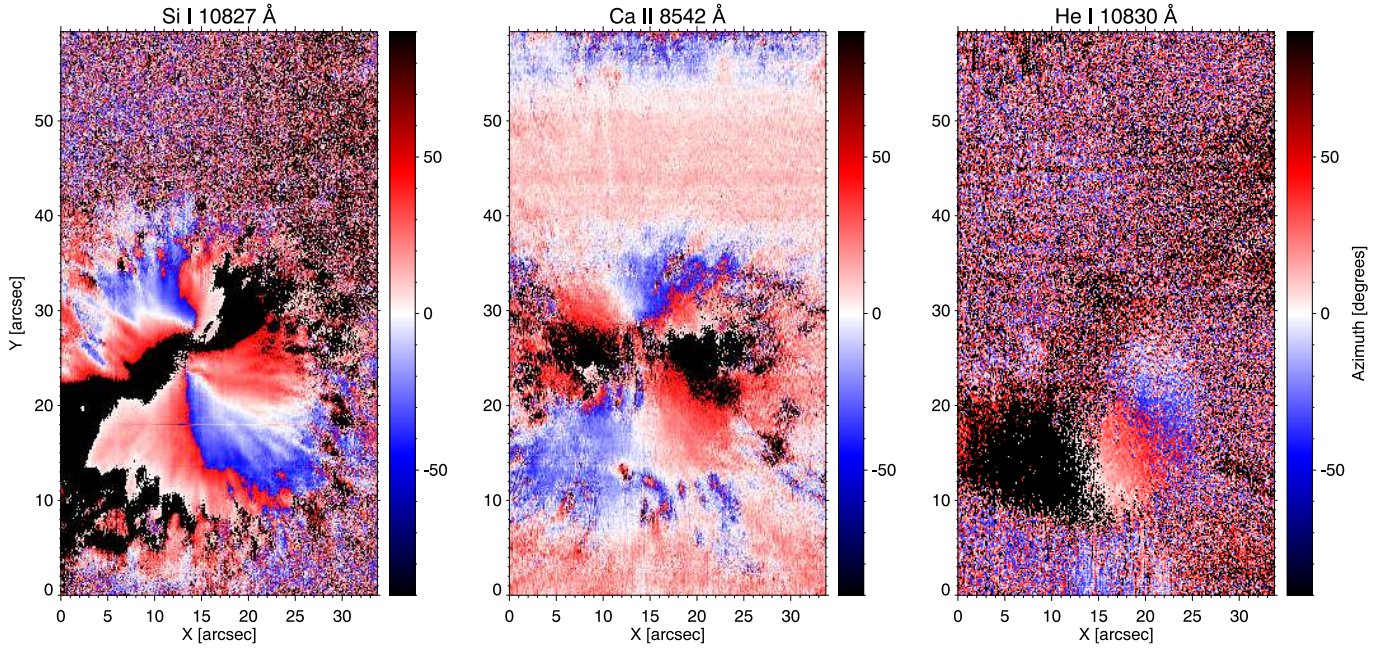

Fig. 14. Spatial distribution of the magnetic field azimuth in the plane of the sky inferred with Eq. (8b) for the Si I line at 10827 Å (left), the Ca II line at 8542 Å (middle), and the He I line at 10830 Å (right). The wavelength ranges considered in the calculation are indicated in the text, and we have used only the line centre range for the Ca II line for this plot.

of the solar atmosphere. In the future, a third spectral channel at 770 nm will be added, covering the K I D_1 line, which probes a range of heights complementary to the currently available channels (Quintero Noda et al. 2017). In addition, while the observations shown in this work were acquired by scanning with the long-slit, the GRIS instrument is also equipped with an integral field unit based on image slicers, which will be offered to observers starting the first semester of 2025. This upgrade to GRIS will lead to new and exciting research.

In this work, we inferred some plasma properties, namely the longitudinal component of the velocity and the magnetic field vector, at several heights in the solar atmosphere by applying simple inference techniques to the observed spectra. Inferring the stratification of these quantities has been possible with the upgraded GRIS thanks to the simultaneous observation of spectral lines formed at different heights in the solar atmosphere. The results of the inference with these simple techniques are consistent with the current knowledge regarding the typical magnetic field vector in sunspots (see, for instance, the reviews of Solanki 2003; Borrero & Ichimoto 2011; Bellot Rubio & Orozco Suárez 2019), giving us confidence in the good performance of the instrument during the commissioning season.

However, properly exploiting these new data requires performing non-local thermodynamic equilibrium inversions of the Si I and Ca II lines. Moreover, several photospheric atomic and molecular lines are present in the observed spectra and can be helpful to constrain better the inversions in the deepest layers of the photosphere. In a follow-up work, we plan to perform such inversions in the observed FOV, analysing in further detail the ensuing inferred stratification of physical quantities.

Acknowledgements. We thank the Gregor team, particularly the campaign's observing assistant, Jürgen Rendtel, for helping perform this observation and obtain such high-quality data. C. Quintero Noda, J. C. Trelles Arjona, T. del Pino Alemán, and M. J. Martínez González, acknowledge support from the Agencia Estatal de Investigación del Ministerio de Ciencia, Innovación y Universidades (MCIU/AEI) under grant "Polarimetric Inference of Magnetic Fields" and the European Regional Development Fund (ERDF) with reference PID2022-136563NB-I00/10.13039/501100011033. The publication is part of Project ICTS2022-007828, funded by MICIN and the European Union NextGenerationEU/RTRP. T. del Pino Alemán's participation in the publication is part of the Project RYC2021-034006-I, funded by MICIN/AEI/10.13039/501100011033, and the European Union "NextGenerationEU"/RTRP. T. Felipe acknowledges grants PID2021-127487NB-I00, CNS2023-145233 and RYC2020-030307-I funded by MCIN/AEI/10.13039/501100011033.

References

Anan, T., Jaeggli, S., Lin, H., et al. 2024, in Society of Photo-Optical Instrumentation Engineers (SPIE) Conference Series, Vol. 13096, Ground-based and Airborne Instrumentation for Astronomy X, ed. J. J. Bryant, K. Motohara, & J. R. D. Vernet, 1309626
Asensio Ramos, A., Trujillo Bueno, J., & Landi Degl'Innocenti, E. 2008, ApJ, 683, 542
Beck, C., Khomenko, E., Rezaei, R., & Collados, M. 2009, A&A, 507, 453
Beck, C., Rezaei, R., Choudhary, D. P., et al. 2018, Sol. Phys., 293, 36
Beckers, J. M. & Tallant, P. E. 1969, Sol. Phys., 7, 351
Bellot Rubio, L. & Orozco Suárez, D. 2019, Living Reviews in Solar Physics, 16, 1
Borrero, J. M. & Ichimoto, K. 2011, Living Reviews in Solar Physics, 8, 4
Calcines, A., López, R. L., & Collados, M. 2013, Journal of Astronomical Instrumentation, 2, 1350007
Cavallini, F. 2006, Sol. Phys., 236, 415
Centeno, R. 2018, ApJ, 866, 89
Centeno, R., Collados, M., & Trujillo Bueno, J. 2006, ApJ, 640, 1153
Centeno, R., Collados, M., & Trujillo Bueno, J. 2009, ApJ, 692, 1211
Collados, M., Lagg, A., Díaz Garcí A, J. J., et al. 2007, in Astronomical Society of the Pacific Conference Series, Vol. 368, The Physics of Chromospheric Plasmas, ed. P. Heinzel, I. Dorotovič, & R. J. Rutten, 611
Collados, M., López, R., Páez, E., et al. 2012, Astronomische Nachrichten, 333, 872
de la Cruz Rodríguez, J., Rouppe van der Voort, L., Socas-Navarro, H., & van Noort, M. 2013, A&A, 556, A115
de la Cruz Rodríguez, J. & van Noort, M. 2017, Space Sci. Rev., 210, 109
de Wijn, A. G., Casini, R., Carlile, A., et al. 2022, Sol. Phys., 297, 22
del Toro Iniesta, J. C., Orozco Suárez, D., Álvarez-Herrero, A., et al. 2025, arXiv e-prints, arXiv:2502.08268
Delbouille, L., Roland, G., & Neven, L. 1973, Atlas photometrique du spectre solaire de [lambda] 3000 a [lambda] 10000
Dominguez-Tagle, C., Collados, M., Lopez, R., et al. 2022, Journal of Astronomical Instrumentation

Felipe, T., Socas-Navarro, H., & Przybylski, D. 2018, A&A, 614, A73
French, R. J., Bogdan, T. J., Casini, R., de Wijn, A. G., & Judge, P. G. 2023, ApJ, 945, L27
Henriques, V. M. J., Mathioudakis, M., Socas-Navarro, H., & de la Cruz Rodríguez, J. 2017, ApJ, 845, 102
Iglesias, F. A. & Feller, A. 2019, Optical Engineering, 58, 082417
Jaeggli, S. A., Lin, H., Onaka, P., et al. 2022, Sol. Phys., 297, 137
Joshi, J. & de la Cruz Rodríguez, J. 2018, A&A, 619, A63
Kentischer, T. J., Schmidt, W., Sigwarth, M., & Uexkuell, M. V. 1998, A&A, 340, 569
Khomenko, E. & Collados, M. 2015, Living Reviews in Solar Physics, 12, 6
Khomenko, E. V., Collados, M., Solanki, S. K., Lagg, A., & Trujillo Bueno, J. 2003, A&A, 408, 1115
Kleint, L., Berkefeld, T., Esteves, M., et al. 2020, A&A, 641, A27
Kuckein, C., Martínez Pillet, V., & Centeno, R. 2012, A&A, 539, A131
Lagg, A., Solanki, S. K., Doerr, H. P., et al. 2016, A&A, 596, A6
Landi Degl'Innocenti, E. & Landolfi, M. 2004, Polarization in Spectral Lines, Vol. 307
Leenaarts, J., van Noort, M., de la Cruz Rodríguez, J., et al. 2025, A&A, 696, A3
Leka, K. D. 1997, ApJ, 484, 900
Löfdahl, M. G. 2002, in Society of Photo-Optical Instrumentation Engineers (SPIE) Conference Series, Vol. 4792, SPIE, ed. P. J. Bones, M. A. Fiddy, & R. P. Millane, 146–155
Martínez González, M. J., Collados, M., Ruiz Cobo, B., & Solanki, S. K. 2007, A&A, 469, L39
Martínez González, M. J., Manso Sainz, R., Asensio Ramos, A., et al. 2015, ApJ, 802, 3
Martínez González, M. J., Manso Sainz, R., Asensio Ramos, A., & Belluzzi, L. 2012, MNRAS, 419, 153
Martínez Pillet, V., Del Toro Iniesta, J. C., Álvarez-Herrero, A., et al. 2011, Sol. Phys., 268, 57
Maurya, R. A., Chae, J., Park, H., et al. 2013, Sol. Phys., 288, 73
Mein, P., Malherbe, J. M., Sayède, F., et al. 2021, Sol. Phys., 296, 30
Orozco Suárez, D., Asensio Ramos, A., & Trujillo Bueno, J. 2014, A&A, 566, A46
Orozco Suárez, D., Asensio Ramos, A., & Trujillo Bueno, J. 2015, ApJ, 803, L18
Pesnell, W. D., Thompson, B. J., & Chamberlin, P. C. 2012, Sol. Phys., 275, 3
Puschmann, K. G., Denker, C., Kneer, F., et al. 2012, Astronomische Nachrichten, 333, 880
Quintero Noda, C., Collados, M., Regalado Olivares, S., & et al. 2024a, in Ground-based and Airborne Telescopes X, Vol. 13094-90, International Society for Optics and Photonics (SPIE)
Quintero Noda, C., Collados, M., Trelles Arjona, J. C., & et al. 2024b, in Ground-based and Airborne Telescopes X, Vol. 13094-103, International Society for Optics and Photonics (SPIE)
Quintero Noda, C., Schlichenmaier, R., Bellot Rubio, L. R., et al. 2022, A&A, 666, A21
Quintero Noda, C., Shchukina, N. G., Asensio Ramos, A., et al. 2024c, A&A, 692, A169
Quintero Noda, C., Shimizu, T., de la Cruz Rodríguez, J., et al. 2016, MNRAS, 459, 3363
Quintero Noda, C., Uitenbroek, H., Katsukawa, Y., et al. 2017, MNRAS, 470, 1453
Rayrole, J. 1967, Annales d'Astrophysique, 30, 257
Regalado Olivares, S., Collados, M., & et al. 2024, in Advances in Optical and Mechanical Technologies for Telescopes and Instrumentation VI, Vol. 13100-206, International Society for Optics and Photonics (SPIE)
Rimmele, T. R., Warner, M., Keil, S. L., et al. 2020, Sol. Phys., 295, 172
Schad, T. A., Penn, M. J., & Lin, H. 2013, ApJ, 768, 111
Scharmer, G. 2017, in SOLARNET IV: The Physics of the Sun from the Interior to the Outer Atmosphere, 85
Scharmer, G. B., Narayan, G., Hillberg, T., et al. 2008, ApJ, 689, L69
Scherrer, P. H., Schou, J., Bush, R. I., et al. 2012, Sol. Phys., 275, 207
Schmidt, W., Bell, A., Halbgewachs, C., et al. 2014, in Ground-based and Airborne Instrumentation for Astronomy V, ed. S. K. Ramsay, I. S. McLean, & H. Takami, Vol. 9147, International Society for Optics and Photonics (SPIE), 124 – 136
Schmidt, W., von der Lühe, O., Volkmer, R., et al. 2012, Astronomische Nachrichten, 333, 796
Socas-Navarro, H., Trujillo Bueno, J., & Ruiz Cobo, B. 2001, ApJ, 550, 1102
Solanki, S. K. 2003, A&A Rev., 11, 153
Solanki, S. K., Barthol, P., Danilovic, S., et al. 2010, ApJ, 723, L127
Solanki, S. K., del Toro Iniesta, J. C., Woch, J., et al. 2020, A&A, 642, A11
Solanki, S. K., Lagg, A., Woch, J., Krupp, N., & Collados, M. 2003, Nature, 425, 692
Stix, M. 1989, The Sun. an Introduction
Trujillo Bueno, J. & Asensio Ramos, A. 2007, ApJ, 655, 642
Trujillo Bueno, J. & del Pino Alemán, T. 2022, ARA&A, 60, 415
van Noort, M., Bischoff, J., Kramer, A., Solanki, S. K., & Kiselman, D. 2022, A&A, 668, A149
van Noort, M., Rouppe van der Voort, L., & Löfdahl, M. G. 2005, SoPh, 228, 191
von der Lühe, O. 1998, New A Rev., 42, 493